A large-scale demonstration and sustainability evaluation of ductile-porous vascular networks for self-healing concrete

Shields, Yasmina; di Summa, Davide; Ospitia, Nicolas; Herrier, Gontran; Schlangen, Erik; Jefferson, Tony; De Belie, Nele; Van Tittelboom, Kim

DOI
10.1016/j.jobe.2024.110040

Publication date
2024

Document Version
Final published version

Published in
Journal of Building Engineering

Citation (APA)
Shields, Y., di Summa, D., Ospitia, N., Herrier, G., Schlangen, E., Jefferson, T., De Belie, N., & Van Tittelboom, K. (2024). A large-scale demonstration and sustainability evaluation of ductile-porous vascular networks for self-healing concrete. *Journal of Building Engineering*, *95*, Article 110040. https://doi.org/10.1016/j.jobe.2024.110040

Journal of Building Engineering 95 (2024) 110040

Contents lists available at ScienceDirect

Journal of Building Engineering

journal homepage: www.elsevier.com/locate/jobe

A large-scale demonstration and sustainability evaluation of ductile-porous vascular networks for self-healing concrete

Yasmina Shields [a], Davide di Summa [a,b], Nicolas Ospitia [a,c], Gontran Herrier [d], Erik Schlangen [e], Tony Jefferson [f], Nele De Belie [a,*], Kim Van Tittelboom [a]

[a] Magnel-Vandepitte Laboratory, Department of Structural Engineering and Building Materials, Faculty of Engineering and Architecture, Ghent University, Ghent, Belgium
[b] Politecnico di Milano, Department of Civil and Environmental Engineering, Milan, Italy
[c] Department Mechanics of Materials and Constructions (MeMC), Vrije Universiteit Brussel (VUB), Brussels, Belgium
[d] BESIX NV/SA, Brussels, Belgium
[e] Delft University of Technology, Faculty of Civil Engineering & Geosciences - Section of Materials & Environment, Delft, the Netherlands
[f] School of Engineering, Cardiff University, Wales, UK

A B S T R A C T

Self-healing cementitious materials show potential to reduce material consumption, maintenance costs, and environmental impacts within the construction sector. This study explores the feasibility of installing a ductile-porous vascular network in a series of retaining walls under realistic construction conditions, with the objective of both assessing the efficacy of the self-healing system and addressing any constructability issues that may arise. Numerical modelling was performed first to determine a suitable mix design and wall configuration that would promote cracking, so cracks would appear without mechanical intervention. The predicted crack distribution informed the optimal network configuration. Healing and sustainability considerations are discussed, and the benefits of implementing this technology are evaluated. When comparing a single maintenance activity using a vascular network versus manual repair, there is no significant benefit of using a vascular network. However, environmental impacts are substantially reduced when using a vascular network once multiple repair actions are considered.

1. Introduction

Vascular self-healing concrete is a promising technique to autonomously repair a structure, and can reduce disruptions to the public due to repair works as well as promote sustainable infrastructure practices. Brittle vascular networks are the most commonly used type of vascular network in the scope of self-healing concrete research [1–8], and are generally 3D printed with polylactic acid (PLA) [2,4,9] or acrylonitrile butadiene styrene (ABS) [6] in the vertical direction to induce weak tensile properties. When a crack is induced in concrete where an embedded brittle vascular network is present, the vascular network breaks along with the concrete, allowing for a healing agent to flow from the vascular network to fill in the crack (as shown in Fig. 1).

The delicate nature of brittle vasculature makes them unsuitable for large-scale applications, as it is difficult to handle them onsite and they are prone to damage during casting. While a self-consolidating mix design can be employed to mitigate the risk of network damage from vibration, this solution incurs additional costs [10,11] and does not address the challenge of managing a lengthy and fragile network on-site. Additionally, brittle vascular networks require support materials during 3D printing, thus requiring additional material and power consumption.

A ductile-porous vascular network incorporates holes that are temporarily plugged with gelatin; the gelatin is dissolved by the

* Corresponding author.
E-mail addresses: yasmina.shields@ugent.be (Y. Shields), Nele.DeBelie@UGent.be (N. De Belie).

https://doi.org/10.1016/j.jobe.2024.110040
Received 13 March 2024; Received in revised form 17 May 2024; Accepted 22 June 2024
Available online 23 June 2024

alkaline environment of the surrounding fresh concrete mix upon casting and curing. These networks would flex upon bending, rather than fracture, and de-bond from the matrix (Fig. 1). This allows a pressurized healing agent to flow through the holes, into the newly-formed gaps around the network, and ultimately to the crack. This new network type offers additional benefits over brittle vascular networks, namely its fabrication involves less material waste and requires less time, and can withstand standard construction activities.

A ductile-porous vascular network is employed in this investigation, given its suitability for scaling-up and addressing challenges associated with fabricating brittle vascular networks [9,12]. A number of large-scale site trials using vascular self-healing concrete have been performed for brittle vascular networks [13–16], however none so far have demonstrated the suitability of scaling up a ductile-porous vascular network, and only two works so far have shown the efficiency of ductile-porous vascular networks at a lab-scale [9,12].

In this study, ductile-porous vascular networks were embedded in a series of retaining walls. In order to demonstrate healing, cracks needed to be formed in the walls. Unconventionally, deliberate efforts were made during the planning and construction process to induce cracks in the concrete walls to eliminate the need for mechanically loading on-site or transporting a large structure to the laboratory for crack creation. Techniques such as excessive cement usage, minimal reinforcement, absence of horizontal reinforcement, rapid formwork removal, and other non-standard building conditions were considered. These techniques were simulated using a combined structural and hygro-thermal analysis with LUSAS to predict the crack sizes and locations within the walls and guide the design of the vascular network.

Early-age hygro-thermal analysis considers hydration, along with creep and shrinkage. Hydration is an exothermic chemical reaction during concrete curing that releases a substantial amount of heat. During this chemical reaction, water and cement react to form hydrates or hydration products, releasing heat at peak temperatures of approximately 40–60 °C (even higher peak temperatures for mass concrete applications). While structural concrete is normally designed to restrict or prevent crack formation, increased cracking is desirable for this study in order to demonstrate the healing capabilities of an embedded vascular network. The risk of cracking generally increases when there are increases in cement content, placing temperature, element thickness, and/or restraints [17].

The purpose of this study is to perform a first demonstration on the viability of scaling up this ductile-porous vascular network for self-healing concrete, as well as to determine any constructability issues that may arise during realistic construction conditions that differ from a controlled laboratory environment. Nine large scale retaining walls were produced on an active construction site in Zaventem, Belgium in Spring 2023. The demonstrator walls were located on the Henneaulaan Bridge Replacement project site with Besix as the general contractor, adhering to real construction-site operational conditions. The site was selected due to its availability of necessary resources such as formwork materials, labor, ample space, and convenient concrete delivery. Embedded sensors monitored curing and strain development of the walls, and microscopy and ultrasonic pulse velocity measurements were utilized to evaluate crack sizes and behavior. Selected cores were extracted from the vascularized walls after they were pumped with a water repellent healing agent and a capillary water absorption test was performed on these cores to give an indication of sealing efficiency. Finally, a life cycle assessment is presented that compares the environmental impacts of a self-healing concrete wall with an embedded vascular network to a traditional wall that is repaired manually.

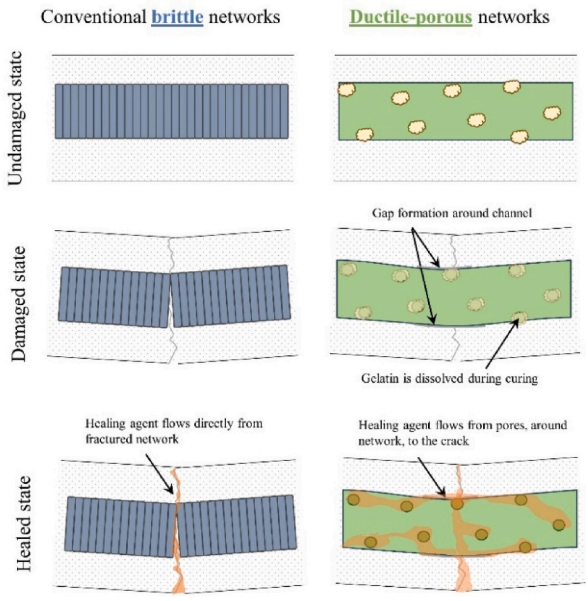

Fig. 1. Depiction of how healing agents are released in either conventional brittle networks or ductile-porous networks.

2. Materials and methods

2.1. Concrete specifications and simulations to promote cracking

A hygro-thermal and structural analysis was performed using the LUSAS concrete material model [18] to compute the thermal and shrinkage strains, with the goal of producing cracks that can later be healed with a vascular network. The crack distribution simulated by LUSAS was then used in order to design and place the vascular networks in the optimal position as well as to estimate the resulting crack widths. The software computes the rate of internal heat generation based on the methodology published by Schindler and Folliard [19], and also simulates creep, autogenous and drying shrinkage, as well as the change in mechanical properties due to hydration [20,21].

The wall geometry was made based on the dimensions of a previous demonstrator by Kheir et al. [22], where a thin wall was cast on an aged restraining base slab to study the early age autogenous shrinkage in an ultra-high-performance concrete. In this study, wall dimensions of 0.1 × 1 × 2 m^3 (thickness x height x length) were selected and the base slab dimensions were 0.2 × 0.95 × 2 m^3 (thickness x width x length). The mix components from Kheir's work were not all available from the concrete supplier, thus an alternative mix composition was developed and verified using numerical modelling. The mix and wall dimensions were informed by the LUSAS model as well as from input on material availability by the concrete supplier, with the final design using the mixes listed in Table 1. Four cubes were cast from the mix of the demonstrator wall with dimensions of 100 × 100 × 100 mm^3 and resulted in an average compressive strength of 58.9 MPa (standard deviation = 1.81 MPa) at 28 days in accordance with EN 12390–3.

The wall geometry and reinforcement details are shown in Fig. 2. The slab reinforcement consisted of two reinforcement meshes (top and bottom) with a 150 mm spacing, 8 mm diameter, and a concrete cover of 25 mm. The base slabs were cast in February 2023 using the mix composition listed in Table 1 for the demonstrator slabs, a vibrating needle was used across the slabs for approximately 30 s. After curing, the vertical wall reinforcement bars of 12 mm diameter were drilled and epoxied in place using the configuration shown in Fig. 2 (with a Young's modulus equal to 200 GPa). After three months of aging, the walls were cast directly on the base slabs. Due to the lack of space within the formwork, the vibrating needle would not fit and was instead placed at the exterior of the formwork. Vibration lasted 30 s and was performed at three locations across the wall.

For the model, a mesh size of approximately 10 × 10 × 10 cm^3 was used to discretize the volume of the wall using trilinear hexahedral elements. During the month of May for the past three years, Brussels had an average temperature of 20 °C and a relative humidity between 65 and 75 % [23]. Conservative values were assumed for the analysis, with initial thermal and environmental conditions taken to be 15 °C and 80 % relative humidity (higher temperature and lower relative humidity resulted in larger cracks widths and earlier crack formation in the LUSAS model).

Since environmental conditions such as temperature cannot be controlled on a construction site, a range of values for different parameters was explored within LUSAS by adjusting the Portland cement content (700–780 kg/m^3), water to cement ratio (0.20–0.50), wall thickness (5–15 cm), restraints (wall length of 1 or 2 m), and formwork removal time (18–36 h). The aim was to find the best combination that promotes cracking.

A two-part staged loading was implemented to account for the change of environmental conditions after formwork removal (Table 2). Assuming an early afternoon casting, the earliest time that was possible to remove the formwork on-site was the following morning, or 18 h later. The analysis would start at the time of casting the wall on top of the existing base slab. Time steps of 1 h were used for the first 24 h in the analysis, followed by time steps of 4 h for the next 36 h, and time steps of 10 h until a 250 h period was reached. Fixed supports were assigned at the bottom surface of the slab to model the soil to slab boundary conditions. A nonlinear incremental iterative full Newton algorithm, along with a fast parallel direct solver, was invoked for solving the governing equations. A convergence tolerance of 10^{-6} was used for both the L2 norms of iterative displacement and out of balance forces. Additional material properties for the wall concrete are given in Table 3.

2.2. Network design and fabrication

In order to design an efficient and sustainable vascular network [24], optimization was used. Design optimization can minimize one or more criteria while satisfying multiple constraints. Criteria that can be minimized include the volume/mass of the network material, impact that the network has on the concrete structural performance (which is related to cross-sectional area of the network), pressure drop as fluid is distributed from the large supply tubes to the smaller ones, cost, and environmental impacts.

Biology can inspire design as it naturally optimizes its own configurations towards efficient designs. The Hess-Murray law [25] is used for this network design, as it minimizes the energy required for fluid transport. It describes the relationship of parent branch radii

Table 1
Mix design for the demonstrator wall and base slab.

Materials	Wall (kg/m^3)	Base slab (kg/m^3)
Sea sand (0–4 mm)	239	782
Aggregates (2–6 mm)	379	851
Cement (CEM III A 42,5 N LA, Cementir Holding)	780	374
Filler (limestone, Calcitec CM)	300	210
Water	365	161
Superplasticizer (Demula Fluvicon 801)	5	1.5

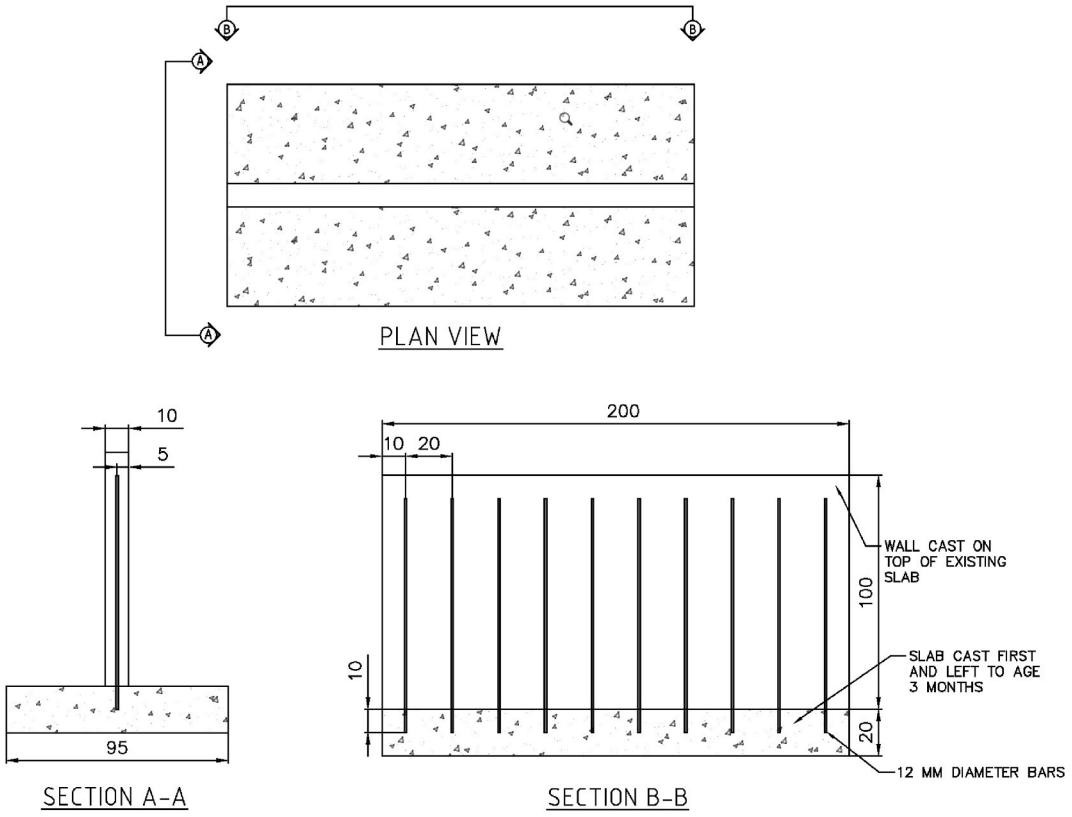

Fig. 2. Wall geometry of the demonstrator wall; dimensions are in cm unless otherwise noted. The base slab reinforcement is not shown for clarity.

Table 2
Environmental conditions for the numerical model.

Property	Value for surfaces exposed to air	Value for formwork surfaces
Environmental temperature	15 °C	15 °C
Convection heat transfer coefficient	20 J/s*m^{2}*°C	7 J/s*m^{2}*°C
Radiation heat transfer coefficient	0.0	0.0
Relative humidity	80 %	80 %
Vapor mass transfer coefficient	−1.0	0

Table 3
Material properties for the wall concrete.

Property	Value
Young's modulus	36 GPa
Poisson's ratio	0.2
Tensile strength	3.5 MPa
Fracture energy per unit area	0.13 N/mm

(r_p) to daughter branch radii (r_d) (**Equation (1)**), as well as the branching angles of blood vessels. This has also been used in previous network configurations in vascular self-healing concrete research [2,4,6,9,26].

$$r_p^3 = r_{d1}^3 + r_{d2}^3 \tag{1}$$

Constraints to be considered for network design include a minimum spacing between branches that is equal to at least the largest aggregate size, to allow the concrete to fully pass through the mold/formwork during casting. The cover from the edge of the network to the edge of concrete should also be restricted to the largest aggregate size, and design should account for existing rebar locations. Minimum channel diameters and wall thicknesses are based on the accuracy of the fabrication technique, and if specified by the project owner, limits on the cost of the chosen materials can constrain the design as well. Additionally, a minimum number of channels across a cross-section should allow for both adequate coverage and sufficient redundancy in case of network blockage.

While 3D printing is very suitable to produce lab-scale vascular networks, the small printing area of most fused deposition modelling (FDM) printers limits the size of a network that can be produced, requiring the construction of smaller parts that are later assembled. To optimize the manufacturing process, pipe extrusion was leveraged for this demonstration to produce the long channels of the vascular networks, which were then attached to a 3D printed branched vascular distribution channel (printing parameters shown in Table 4). The ductile-porous network design involved the use of 3D printed polylactic acid (PLA) branched ends connected to extruded polyurethane (PU) tubes of 1.2 mm thickness, so that the daughter branches would be concentrated at the center of the wall in order to service the main primary crack that was expected to develop there (according to the numerical modelling results). Pores of 1.5 mm were manually drilled in a spiral pattern with a spacing of 10 mm into the 333 mm long PU tubes at the central part of the network (shown in green in Fig. 3). The pores were temporarily plugged by manually applying a layer of gelatin solution (approximately 1 mm thick) to prevent concrete infiltration during casting.

An internal channel diameter of 7 mm was used for the daughter channels, and the internal diameters of the subsequent parent branches were increased in accordance with the Hess-Murray Law so that the subsequent parent branches' internal diameter would increase from 8.8 mm, 11.1 mm, to 14 mm. A wall thickness of 1.2 mm was maintained for all printed parts, which was the minimum allowable wall thickness based on the standard nozzle size that was used for printing. Branching angles of 75° were incorporated in the design, which also followed the Hess-Murray's Law. A spacing of 50 mm center to center between the network channels was used to allow for adequate healing agent coverage based on preliminary lab testing. A concrete cover to the network of 40 mm was maintained, and the network was secured to the reinforcement using tie wire, as shown in Fig. 3.

The branched ends of the network were fabricated using a Bambu Lab X1 Carbon 3D printer; the printing parameters are given in Table 3. These parts were printed horizontally on the build plate. Additionally, instead of a heated build plate with painter's tape to promote adhesion, a Bambu Lab cool plate was implemented which allowed a lower bed plate temperature of 30 °C to be used (typically bed plates are heated to 60 °C).

2.3. Network installation and use of the healing mechanism

Network design must also consider how they will eventually be installed in the field. Ease of installation is necessary for construction, as labor time translates to a significant portion of construction costs, which contractors aim to minimize unless otherwise specified in their contract documents by the owner. Ideally, networks should be installed after the rebars have already been placed in the formwork, so that rebar installers do not need to work around the networks and potentially damage them. The networks for this demonstrator were thus tied directly to the reinforcement, using common steel tie wire that was already available on the construction site.

Six of the nine walls included a vascular network (wall numbers W4–W9); the three remaining walls without a network were designated as the reference walls (wall numbers W1–W3). At an age of 14 days, the networks in the demonstrator walls were filled with approximately 200 mL of water repellent agent (SikaGuard 705 L, Sika, with a viscosity equal to 2.6 mPa s at 20 °C) using a syringe until the fluid emerged from the other end of the vascular network. The end of the vascular network was clamped shut and air was pressurized by a mobile air compressor unit at 10 bars to force the water repellent to travel from the network to the cracks (shown in Fig. 4).

2.4. Monitoring curing and damage

2.4.1. Embedded sensors

Vibrating wire strain gauges (Model EM-5, ROCTEST) were embedded 15 cm from the top and bottom in the center of each demonstrator wall; they were secured in place with tie-wire against the vertical reinforcement as shown in Fig. 5. Based on the numerical modelling results, a main crack was expected to form directly in the center of the wall, thus the strain gauges were installed as such.

The vibrating wire strain gauge contained two end flanges with a stainless-steel tube connecting them, with a tensioned steel wire clamped into the end flanges and axially through the tube. An electromagnet mounted at the center of the steel wire vibrates when deformations in concrete occur, and the vibration frequency of the wire is measured by an external readout unit. The range of the gauges is 3000 μstrains, which corresponds to approximately 0.5 mm of deformation. The total strain is obtained from an initial to a subsequent reading with the following equation:

$$\Delta\varepsilon = \varepsilon_1 - \varepsilon_0 = K \times 10^9 \times \left[\frac{1}{N_1^2} - \frac{1}{N_0^2}\right] \tag{2}$$

Table 4
3D printing processing parameters for the branched ends of the vascular network using a Bambu Lab X1 Carbon 3D printer.

Processing parameter	Value
Layer height (mm)	0.25
Printing speed (mm/sec)	40
Nozzle size (mm)	0.4
Nozzle temperature (°C)	200
Infill (%)	100
Fan speed (%)	100
Bed plate temperature (°C)	30

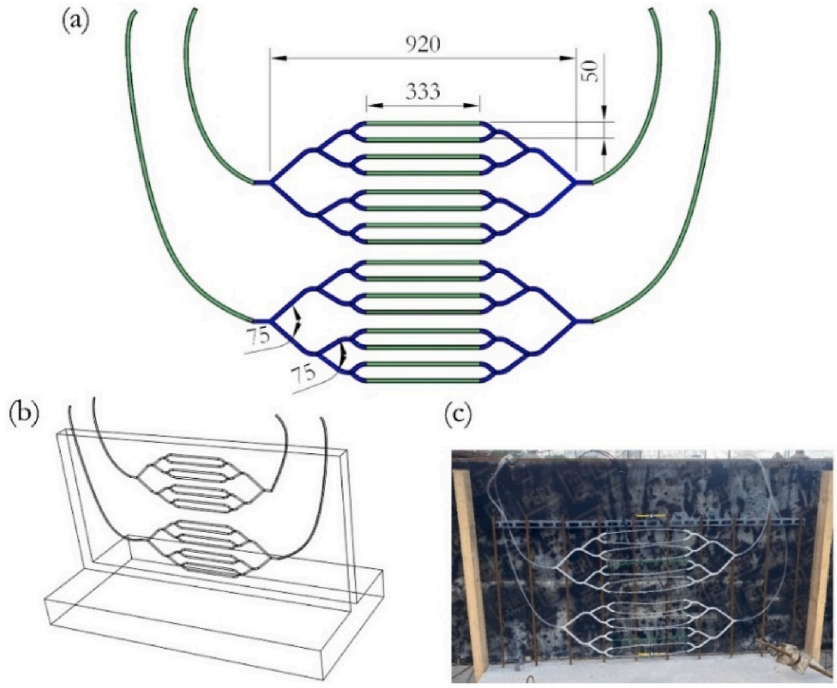

Fig. 3. (a) Network dimensions where PU tubes are shown in green and 3D printed branched parts are shown in purple, (b) network placement in 3D CAD drawing, and (c) on-site conditions. Dimensions are given in mm.

Fig. 4. Supplying the network with water repellent agent; fluid is seen seeping out of the primary crack at the bottom of the wall.

where $\Delta\varepsilon$ is the total strain measurement (μstrains), ε_1 is the current strain measurement (μstrains), ε_0 is the initial strain measurement (μstrains), K is the gauge constant of 4.0624, N_1 is the current period measurement (μsec), and N_0 is the initial period measurement (μsec). Negative strains indicate compression and positive strains indicate tension. Measurements were taken in intervals of 1 h and the data could be accessed from a datalogger that was connected to each cable of the strain gauges.

Thermal sensors (SmartRock3, Giatec) were included in three of the walls and secured to the reinforcement, as shown in Fig. 5. Temperature measurements were recorded at two locations on the sensor, at the cable and at the body, with a reading range of −30 to 85 °C and accuracy of ± 1 °C. Measurements were taken in intervals of 15 min and could be accessed in real time and remotely using the SmartRock mobile app.

2.4.2. Optical microscopy and visual observation

Crack width measurements of the main central crack on the walls were taken in situ using a portable digital microscope (Toolcraft DigiMicro Mobile microscope, 5 MP). To get an average crack width, 5 measurements were taken every 10 cm along the length of the crack (for a total of 50 measurements). Crack width measurements were taken every 24 h for the first 5 days after casting, and then

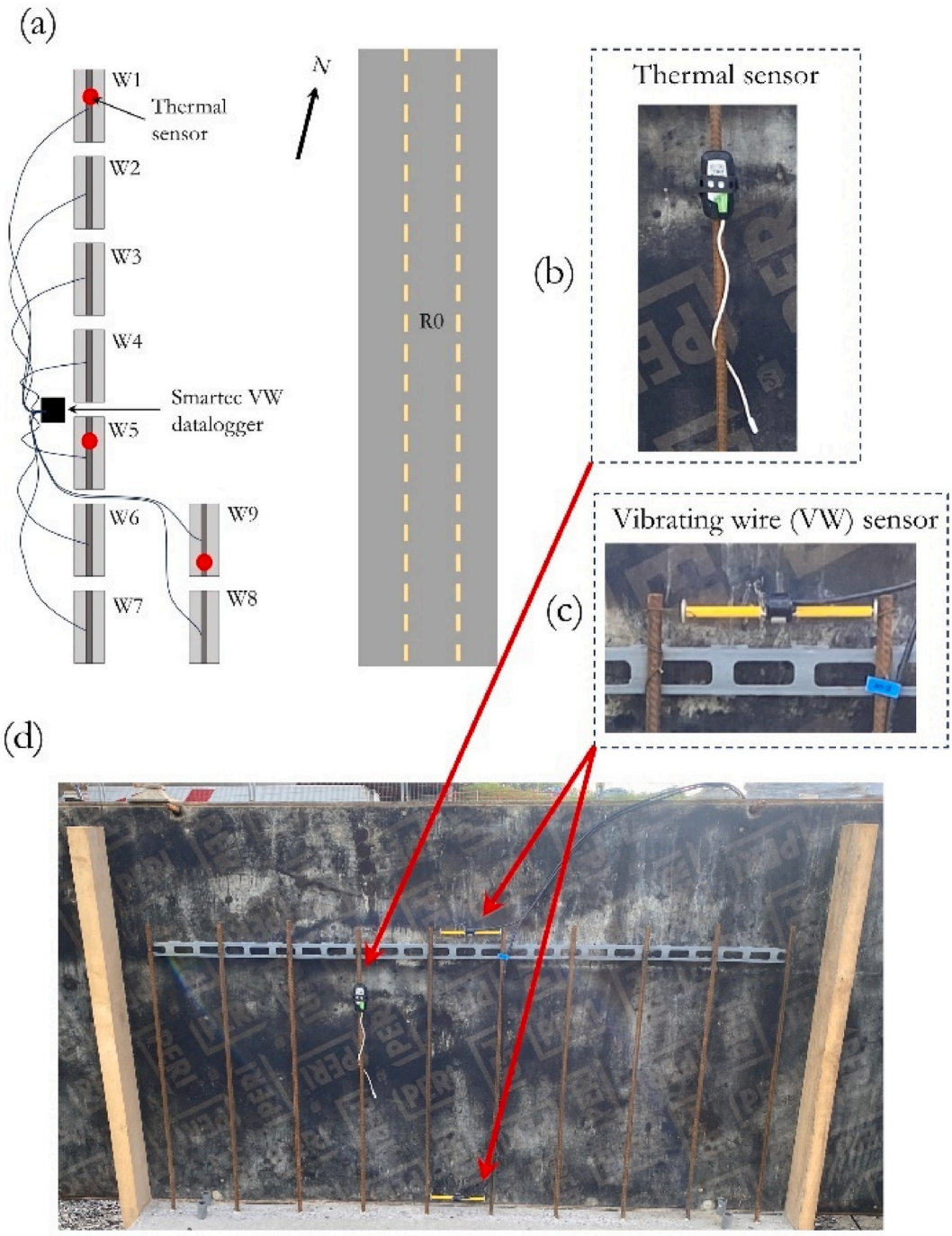

Fig. 5. (a) Demonstrator wall arrangement (numbered W1 thru W9), (b) thermal sensor configuration, (c) vibrating wire sensor configuration, and (d) location of sensors embedded in the demonstrator walls. The walls were located on a project site adjacent to the highway ring of Brussels (R0) in Zaventem, Belgium.

again on day 10.

Representative cores were taken from the walls at the end of the healing process in order to perform a capillary water absorption test in the lab. The core extractions were located over the main central crack of selected walls with a vascular network, over the main central crack of one reference wall, as well as at the top corners of reference wall (where no cracks were present). In total, 15 cores were extracted: three uncracked cores, three reference cracked (without healing) cores, three cracked and partially healed cores, three cracked and fully healed cores, as well as three cracked and unhealed cores (with a vascular network where healing was unsuccessful). Immediately before the test, the crack widths of the cores were verified with a stereomicroscope (Leica S8 APO, with DFC 295 camera).

To get an average crack width, 5 measurements were taken in four zones along the length of the crack at the bottom face of the core that would be in contact with water for the water absorption test (for a total of 20 measurements).

Additionally, at each site visit, a marker was used to trace the cracking patterns on the sides of the walls so that they could be visible in pictures and the damage can be clearly tracked visually over time.

2.4.3. Indirect ultrasonic pulse velocity

The ultrasonic pulse velocity of a representative wall was calculated by measuring the transit time of ultrasonic pulses through the concrete using a Controls PULSONIC portable device, in accordance with ASTM C597. The transmitter and receiver were placed in an indirect (surface) transmission configuration, spaced at a distance of 20 cm between each other across one face of the wall in a grid pattern as shown in Fig. 6. Measurements were taken horizontally in rows across the wall to yield a UPV value between each of the dots marked on the wall. The pulse had a magnitude of 2500 V and frequency of 54 kHz, and the transmitted signal was recorded using a sampling rate of 10 MHz. The transit time (Δt in s) was measured three times to produce an average value, and the ultrasonic pulse velocity (UPV in m/s) was calculated using a wave propagation distance (Δx) of 20 cm.

2.5. Evaluating healing on cores using capillary water absorption

A capillary water absorption test was performed on 100 mm diameter cores extracted from cracked and uncracked positions in the walls after healing agent was pumped through the network. The cores were placed in an oven at 40 °C for a period of 10 days. Samples were then removed from the oven and two coatings of epoxy resin sealer (Episol® Designtop SF) were applied with a brush on the side and bottom surface, keeping a 14 mm wide exposed strip centered on the crack along only the bottom of the specimen. Once the epoxy coating was cured, the samples were returned to the oven at 40 °C for 5 days.

During the capillary water absorption test, the cores were set on two non-absorbing supports in a box containing water, so that they were immersed in water 3 ± 1 mm above the bottom of the specimen. The cores were weighed to determine the weight gain with time after 10 min, 20 min, 30 min, 1 h, 1 h 30 min, 2 h, 3 h, 4 h, 6 h, 8 h, and 24 h. A damp cloth was used to remove excess moisture from the surface of the specimen before recording its mass.

To assess healing of the cracked samples, a sealing efficiency (SE) was calculated with the following equation as per Van Mullem et al. [27]:

$$SE = \frac{\overline{SC}_{REF\ CR} - \overline{SC}_{Healed}}{\overline{SC}_{REF\ CR} - \overline{SC}_{REF\ UNCR}}\ x\ 100\% \tag{3}$$

where SC represents a sorption coefficient obtained from the linear slope line for graphs of cumulative mass gain versus the square root of time. $\overline{SC}_{REF\ CR}$ represents the average SC of the cracked reference series (g/$\sqrt{}$hr), $\overline{SC}_{REF\ UNCR}$ represents the average SC of the uncracked reference series (g/$\sqrt{}$hr), and $\overline{SC}_{Healed}$ represents the average SC of the healed specimens (g/$\sqrt{}$hr).

2.6. Sustainability considerations

The environmental impact of using the vascular network developed in this study is compared to traditional manual repair by injection. The system boundary of this life cycle assessment considers the raw material extraction, processing, transportation and maintenance being undertaken between one and five times during the service life where a water repellent agent is used for the repair of the functional unit, which is considered here to be a 1 m^2 wall area. SimaPro software with the Ecoinvent 3.6 database was used for the analysis, and multiple impact indicators using the CML-IA method were calculated, including: abiotic depletion potential (ADP), global warming potential (GWP), ozone depletion potential (ODP), human toxicity potential (HTP), fresh water aquatic ecotoxicity (FAETP), marine aquatic ecotoxicity (MAETP), terrestrial ecotoxicity potential (TETP), photochemical oxidation (POCP), acidification (AP), and eutrophication (EP).

For manual repair, holes are typically drilled at a 45° angle with a rotary hammer (Fig. 7) (with a wattage of 850 W) which are then

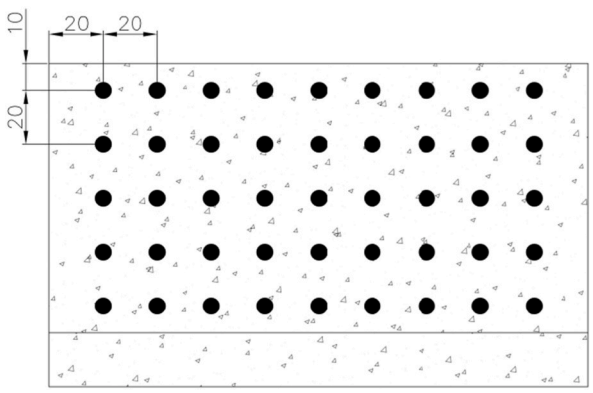

Fig. 6. Grid of points where UPV measurements were taken in rows horizontally across one representative wall; dimensions are given in cm.

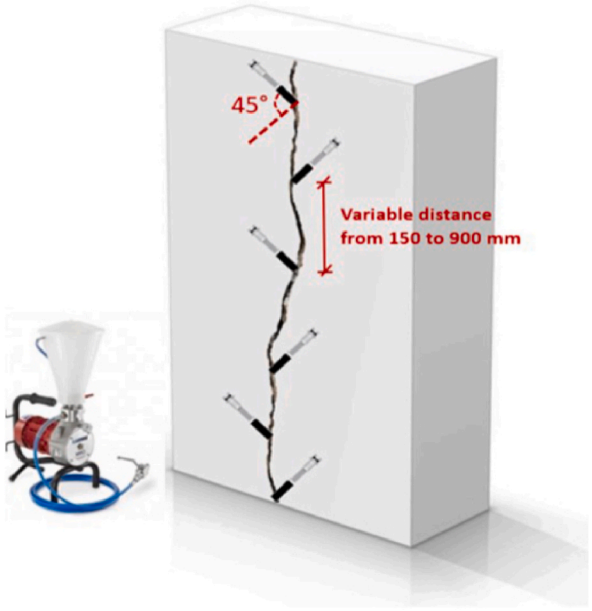

Fig. 7. Depiction of traditional manual repair process for a concrete wall, where holes are drilled at 45° angles and subsequently injected with a repair fluid using a pump (figure taken with permission from Ref. [28]).

pumped with a healing agent using a pump (with a wattage of 750 W) [28]. To service the main crack at the center of the demonstrator wall, 0.5 h of drilling, 1 h of pumping, and 100 g of water repellent agent are estimated.

For the wall with an embedded vascular network, a maximum power output of 1000 W is listed on the Bambu Lab X1 Carbon 3D printer data sheet. However, when measured during printing, this power output was only achieved during the warm-up period if the heated bed-plate was being used and set to at least 60 °C. Since a high temperature bed plate setting was not used for the production of the 3D printed branched parts of the vascular network, this maximum power output was not observed. During printing, the power draw for printing PLA was between 95 and 140 W; an average power consumption of 118 W is then assumed for the total duration of printing. For comparison, the environmental impacts of nylon and polypropylene filaments are considered as well; since these materials require both higher extrusion temperatures and longer printing times, an increase in 30 % of power consumption and printing time is assumed. Acrylonitrile butadiene styrene (ABS) is also considered, and this has similar temperature and printing time requirements as PLA.

For extrusion processing of the straight tubes in between the 3D printed branches as well as the tubes connecting the network to the outside of the concrete element, power consumption is generally between 0.08 and 1 kW h per kg output [29,30] depending on the screw speed [31]. An average value of 0.54 kW h/kg is assumed.

The network designed for this study encompasses roughly a 1 m^2 area of wall, and the portion that is analyzed can be assumed to be located in an area that is difficult to access, such as a tunnel wall, where the transportation of a scissor lift would be required to allow access for manual repair (this would not be needed for a vascular network); a Genie GS1932 electric scissor lift is considered. A full battery recharge is assumed, which is required for transportation across a work site for each maintenance activity, that takes 6–8 h for a full recharge [32,33]. Impacts of the 3D printer itself and power tools used for repair by manual injection are considered negligible since they are used multiple times. The power consumption, raw material quantities and equipment usage associated with vascular

Table 5
Materials, power consumption, and transportation distances for vascular network production and one healing action.

Item	Material	Equipment	Material quantity	Wattage	Time	Power consumption	Distance for transportation
3D printed parts	PLA	3D printer	248 g	118 W	9.3 h	1.1 kW h	50 km
	ABS[a]	3D printer	248 g	118 W	9.3 h	1.1 kW h	50 km
	PP[a]	3D printer	248 g	153 W	12.1 h	1.9 kW h	50 km
	Nylon[a]	3D printer	248 g	153 W	12.1 h	1.9 kW h	50 km
Extruded tubes	PU	Extruder	215 g	–	–	0.1 kW h	50 km
Gelatin powder	–	–	20 g	–	–	–	20 km
Pump	–	Pump	–	750 W	0.1 h	0.1 kW h	100 km
Transport of assembled vascular network	–	–	–	–	–	–	20 km
Healing agent	WRA	–	200 g	–	–	–	50 km

[a] These materials were not used for the demonstrator but are included as alternatives to PLA or PU for comparison.

network production and repair are included in Table 5 and those associated with traditional repair are included in Table 6.

200 g of water repellent agent was used for the demonstrator walls; a larger quantity of healing agent is necessary for using the vascular networks compared to manual repair, since the healing agent must be completely filling the network first before it is pressurized. Half of this amount is estimated for manual repair works, since repair is done in a localized fashion.

Transportation distances were chosen based on the equipment rental (scissor lift, rotary hammer, and pump) and polymer processing (filaments, extruded tubes, and water repellent agent) companies available throughout Belgium, assuming the site location is still in Zaventem, Belgium. The distances for making the vascular network were conservatively assumed on the basis of the site location being in proximity (20 km) to either a large city or a university, which typically have fabrication labs with 3D printers available to use. Polymer processing facilities are less abundant in a given area and are assumed to be in an industrial area further away from the site location (50 km). It is assumed that the network is assembled at the location of where the 3D printer is, and then transported to the site location.

To estimate the environmental impacts of multiple repair methods using a vascular network, only the quantity of the healing agent and transport and usage of the pump is multiplied by the number of repair works, since the production of the vascular network is only done once. For multiple traditional repair actions, every aspect is multiplied by the number of repair works.

Due to lack of data on the chemical composition and the technical and safety data sheets not disclosing all necessary information, only three indicators were available and thus used for the life cycle inventory of the water repellent agent: global warming potential (GWP), ozone layer depletion (ODP), and abiotic depletion (ADPE). This information was provided by an environmental product declaration sheet for Sika products based on polyurethane or silane-modified polymer [34].

3. Results and discussion

3.1. Crack predictions using numerical modelling

After iteratively changing parameters for the mix design and acquiring feedback from the concrete supplier, the final mix composition resulted in a w/c ratio of 0.5 and a high cement content of 780 kg/m^3. The model developed using LUSAS indicated that the combination of shrinkage and thermal strains would help to promote cracking (Fig. 8). Crack development would start shortly after formwork removal and peak at a maximum crack width of approximately 300 μm.

The contour plots indicating the maximum crack width of each element from the preliminary model are shown in Fig. 9, showing a primary crack forming at the center of the wall and secondary cracks stemming from the base of the wall.

As expected in the numerical model from LUSAS, a primary crack formed in the middle of the walls within the first 24 h of being cast (Fig. 10); the primary crack in walls W4 and W7 formed directly in the center and passed directly through the embedded strain gauges, while the primary cracks in the other walls formed mainly within the middle third of the wall. It is noted that the 'crack width' shown in Fig. 9 is the total inelastic displacement between crack surfaces, which includes both normal and shear displacement components. The latter (shear displacement component) is dominant at the stem-base interface. These predicted interface shear displacements are perhaps larger that expected, since the dowel action of the vertical bars was not included in the model, although the rough crack contact model embedded in the LUSAS concrete model would have limited the shear displacements to some degree.

The presence of the vascular network did not appear to affect the cracking patterns that developed at the surface of the walls. Visual observations revealed that all walls, regardless of whether they featured a vascular network, exhibited nearly identical patterns of cracking. This similarity extended to both the size of the cracks and the patterns of strain development as illustrated in the following section. Measurements and visual assessments confirmed that there was no discernible deviation in crack propagation or distribution between walls with a vascular network and those without. This suggests that the embedment of a vascular network (of this particular geometry) within a concrete element does not compromise its structural integrity nor does it alter the behavior of crack formation.

3.2. Monitoring curing and damage with embedded sensors

The ambient and internal wall temperature during the course of the demonstration is shown in Fig. 11. For clarity, only one of the three instrumented walls is plotted as the differences among them were minimal. A peak temperature between 50 and 55 °C was reached for the walls approximately 10 h after casting, and large temperature fluctuations (which follow the outside temperature after day 1) within the wall are noted.

Deformation measurements in one representative wall are shown in Fig. 12, which confirms visible crack formation between 50 and 100 μm within the first 20 h with the LUSAS model (strain at 20 h was 582 μstrains per the strain gauge sensor, corresponding to 97 μm), and continuously increases as it ages. According to the manufacturer of the vibrating wire strain gauges, it is possible that certain environmental conditions may have a slight effect on the strain measurements, including rainfall, excavation, traffic, temperature, and construction activities nearby. This effect appears to be more than slight, as the strains fluctuate continuously with temperature with a

Table 6
Materials, power consumption, and transportation distances for traditional manual repair (including one healing action).

Item	Material	Equipment	Material quantity	Wattage	Time	Power consumption	Distance for transportation
Drilling holes	–	Rotary hammer	–	850 W	0.5 h	0.2 kW h	100 km
Pumping action	–	Pump	–	750 W	1 h	0.8 kW h	100 km
Healing agent	WRA	–	100 g	–	–	–	50 km
Battery charge for scissor lift	–	Scissor lift	–	771 W	7 h	5.39 kW h	200 km

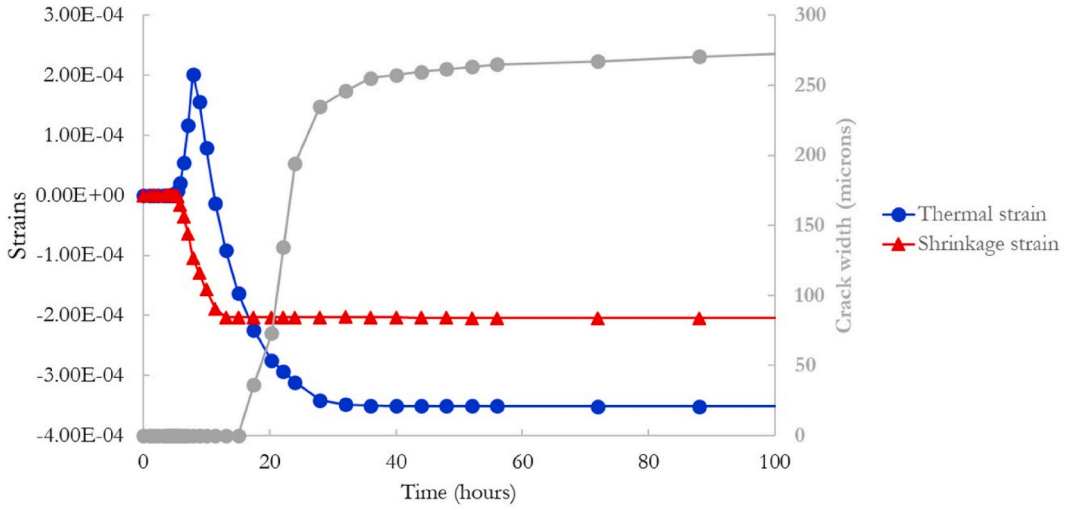

Fig. 8. LUSAS modelling results at a central point in the wall indicating crack widths and strains over the first 100 h, where the cement content was equal to 780 kg/m^3 and w/c ratio to 0.5.

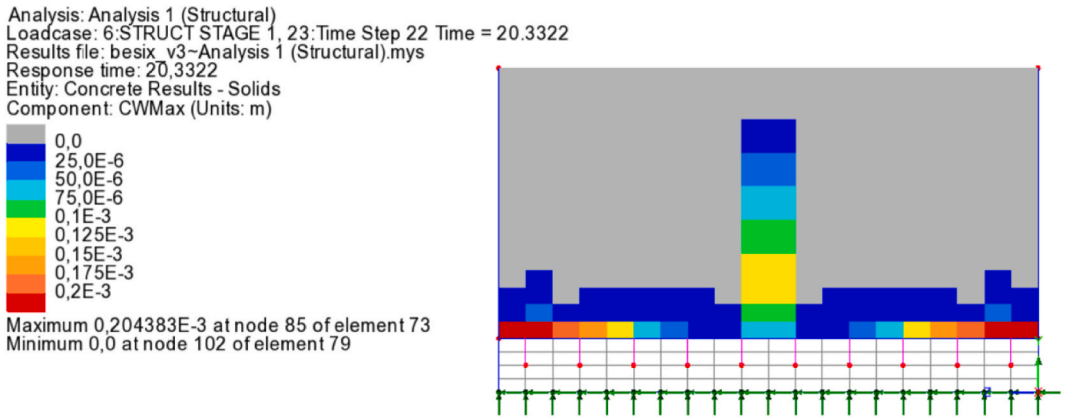

Fig. 9. LUSAS modelling results indicating the crack width contours 20.3 h after casting, where the cement content was equal to 780 kg/m^3 and w/c ratio to 0.5.

range of 200 μstrains throughout the day.

The presence of the vascular networks did not appear to affect the strain development within the walls; all walls with and without a network reached peak strains at approximately 2500 μstrains at the top vibrating wire sensor. For all walls, the top sensor experienced significantly higher strains than at the bottom, due to the restraint that the bottom has from the base slab.

3.3. Indirect ultrasonic pulse velocity

UPV values give an indication of concrete quality and damage that is present and can be categorized by values above 3900 m/s as being uncracked or undamaged concrete, values between 2500 and 3900 m/s as concrete having minor damage and cracking, and below 2500 m/s as being severely damaged concrete [26]. The measured pulse velocities of wall W4 in its damaged state 14 days after casting are projected in the color map shown in Fig. 13. Most of the cracks could be identified with the UPV mapping, and lower UPV values correlated well with corresponding cracks whose widths were relatively larger. The mapping could clearly detect the large main crack at the center of the wall, recording a minimum UPV value of 2443 m/s.

The horizontal cracks at the top of the wall could not be well identified with UPV since the cracks were parallel to the propagation direction of the wave, nonetheless, vertical cracks in between the measuring points showed a high reduction of the UPV. A smaller grid size in addition to measurements taken in the vertical direction can overcome this to provide greater accuracy, however this comes at a cost of a substantially increased execution time.

3.4. Constructability remarks

Unfortunately, during installation of the formwork of demonstrator wall W8, the 3D printed branched portion of the network became damaged (Fig. 14). Although this ductile-porous network can withstand more bending forces than a brittle counterpart, this

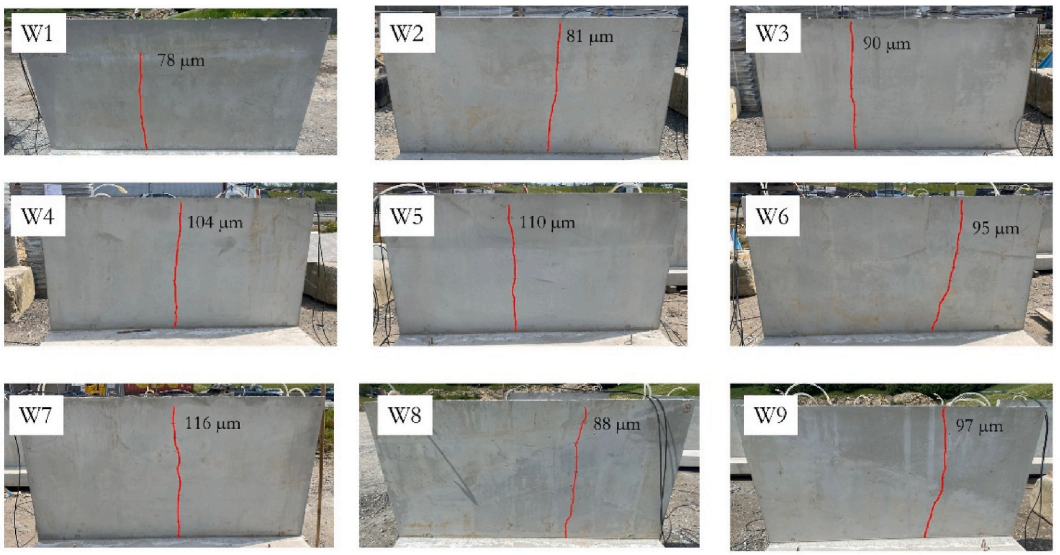

Fig. 10. Primary crack formation in the demonstrator walls the day after casting and their corresponding crack widths.

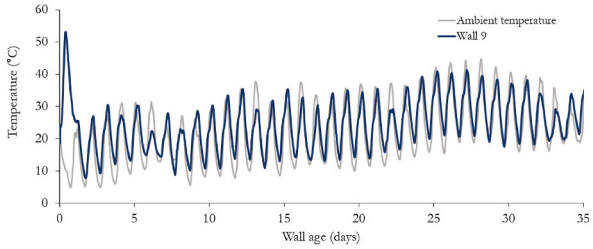

Fig. 11. Ambient temperature and internal temperature of Wall 9.

highlights the need for careful installation onsite to avoid any impact damage.

Of the six walls which included a vascular network, only four could be pumped with the healing agent as two of the walls' networks were completely blocked. Upon inspection of cores that were taken from the walls after the healing period, it was found that some of the extruded tubes of the networks had shifted during casting. Since the connections of the network to the reinforcement were only made on the 3D printed branched portions, it is possible that the denser concrete pushed the network upwards, causing mid-span bending and -in turn-detachment of the gelatin from the channels. More rigid tubing would then be preferable to avoid vascular network deflection/sagging, as well as additional connection points so that the fresh concrete does not displace the vascular network.

Additionally, to make a system truly self-healing would require removing human intervention as much as possible. Embedded sensors to detect damage could be employed that would engage a pump that supplies a healing agent through the network to allow for a fully autonomous process.

3.5. Evaluating healing on cores using capillary water absorption

Three cores were selectively taken from cracked and uncracked locations on the demonstrator walls and grouped into the following categories: uncracked (UNCR), reference cracked (REF CR), vascular network with no healing present (V-unhealed), vascular network with limited healing observed (V-partially healed) and vascular network with excessive flow of healing agent coming from the crack (V-healed). Unfortunately, one core from both the REF CR and V-partially healed series were damaged during transport, so only two repetitions for those series are reported here.

The results of the capillary water absorption test are plotted with the cumulative water absorption over the square root of time in Fig. 15. As expected, the reference cracked series experienced the most capillary water absorption given that they had no healing present, with an average cumulative water uptake of 47.3 g at the end of the 24-h period. The V-unhealed series had similar values to the REF CR-2, as they had similar crack widths (0.34 mm for REF CR-2 and between 0.23 and 0.36 mm for the V-unhealed series). REF CR-1 had a notably larger average crack width (0.54 mm), accounting for its increased capillary water uptake.

The V-partially healed series had similar water uptake behavior to the uncracked specimens, and superior healing performance is seen for the V-healed series, where the average cumulative water uptake was less than 5 g after the test.

The sealing effect can be further described by comparing the sorption coefficients of each series to produce a sealing efficiency as

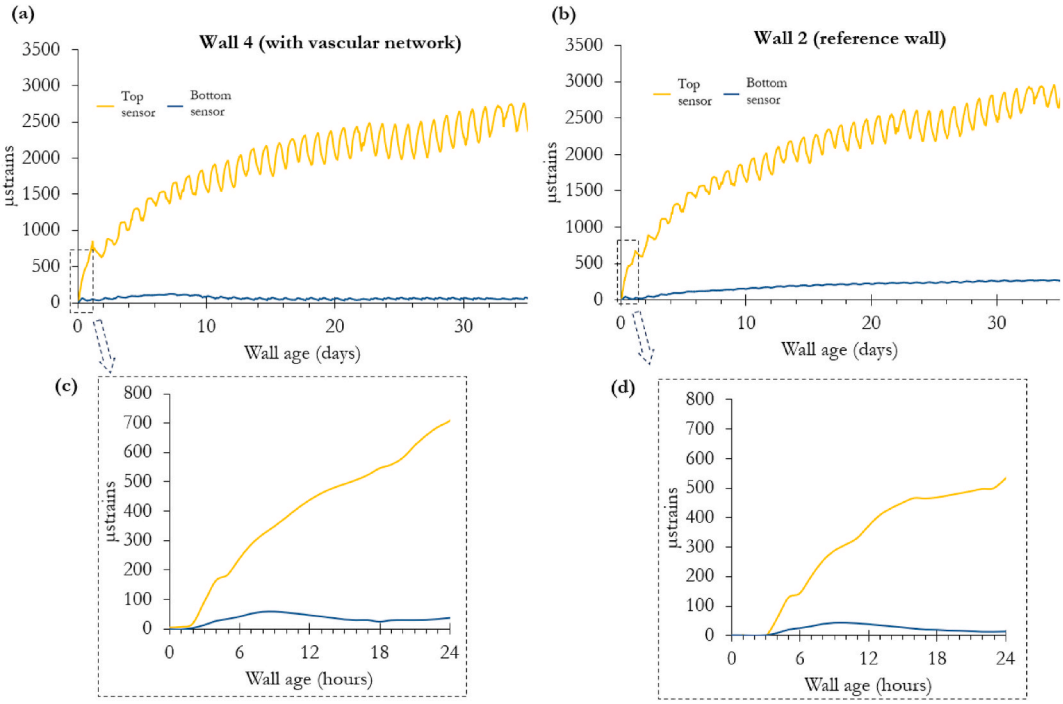

Fig. 12. Deformation measurements recorded by vibrating wire sensors for one representative wall with a vascular network (W4) (a) and one reference wall (W2) (b), as well as a highlight on the first 24 h of age in (c) and (d).

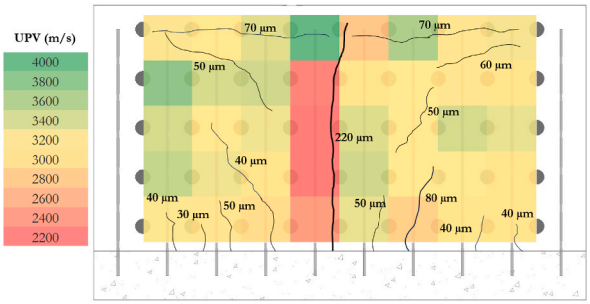

Fig. 13. UPV color map on wall W4 with crack widths overlaid; increasing line thicknesses correspond with increasing crack widths.

given in **Equation (3)**. The sealing efficiencies of the partially healed and fully healed cores are given in Fig. 16. Exceptionally and consistently high sealing efficiencies are noted for the fully healed cores, with an average of 273 % and standard deviation of 9.4 %. Such high efficiencies are possible here as the water repellent agent not only sealed the crack itself but seeped out and sealed the outer surface of the demonstrator wall, making it significantly less permeable than the uncracked cores that were tested. One of the partially healed cores achieved over 100 % sealing efficiency (121 %), while the other had 53 %; their varied crack widths and tortuosity could account for this, as well as more of the vascular channels being blocked and/or displaced during casting for the V1-partially healed sample, as shown in Fig. 17.

3.6. Sustainability considerations

Fig. 18 gives an overview of the different impact indicators that manual repair has compared to vascular networks produced with different potential polymeric materials for one maintenance activity only.

With respect to ozone layer depletion, manual repair had the greatest impact compared to each vascular network material, which is anticipated since this indicator is directly related to environmental effects caused by transportation. Manual injection had the lowest impact in terms of abiotic depletion potential, since it does not involve the extraction of raw materials to the extent that polymer processing does [35,36]. After further maintenance, the impacts related to abiotic depletion potential for manual repair becomes less than those of vascular networks; after 6 repair activities an ABS network becomes more beneficial, and after 13, 16, and 24 activities then a PP, PLA, and nylon network becomes more beneficial than manual repair (Fig. 19).

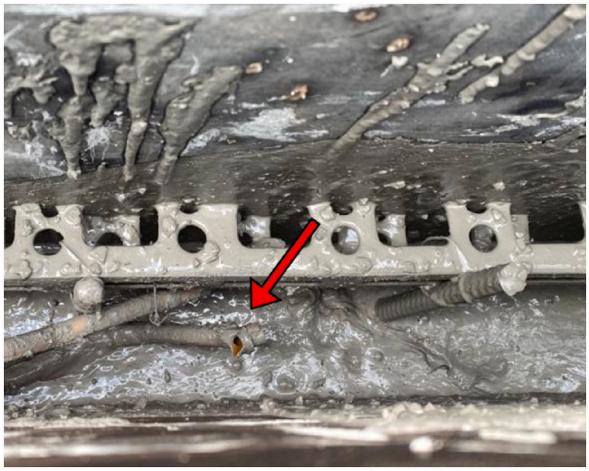

Fig. 14. Image taken from the top of the wall looking down into the formwork; arrow indicates where the network was observed to be damaged.

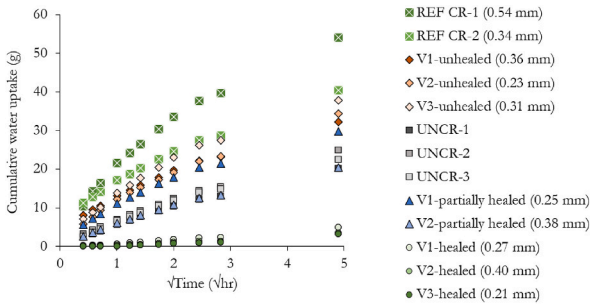

Fig. 15. Capillary water absorption test results on cores showing the cumulative water uptake over the square root of time; corresponding crack widths are shown in parentheses.

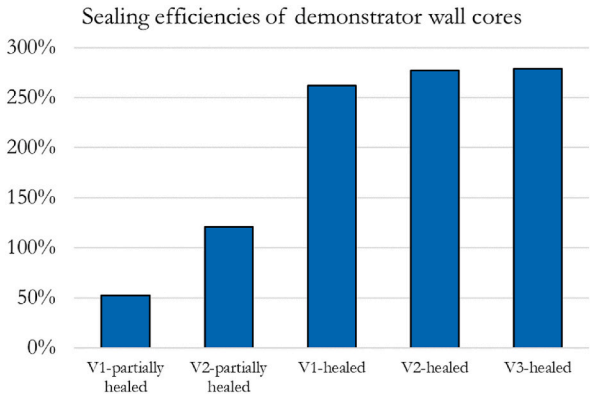

Fig. 16. Sealing efficiencies of individual cores from the demonstrator walls.

Vascular networks with PLA were expected to have the least environmental impact relative to other polymeric filaments given that it is derived from corn rather than fossil fuels, yet in each category its impacts were similar or greater than ABS, nylon, and polypropylene filaments. The processes involved with the production of PLA are more extensive than the other polymers investigated and thus account for the increased impacts that are seen, resulting in a perceived worse overall environmental impact for certain categories.

PLA is a plant-based bioplastic made from either harvested corn or sugar cane. An extraction process follows harvesting to obtain starch from the raw materials, which is dried and then fermented to produce lactic acid. The lactic acid then undergoes a process to polymerize it into polylactic acid resin, which can be done via ring-opening polymerization [37–39]. This entire process to produce

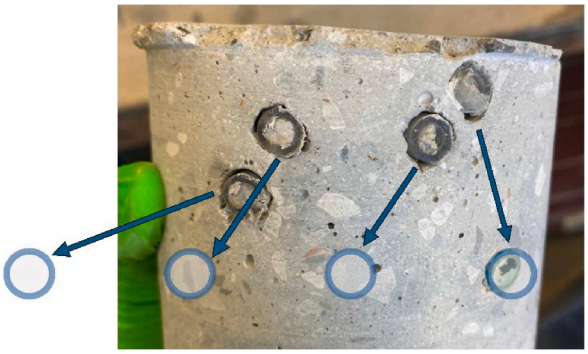

Fig. 17. Core extraction showing misalignment of vascular channels due to displacement during the casting process. The actual positions of the channels are visible as partial obstructions within the core. The intended positions of the channels are indicated by overlaid blue circles, illustrating the deviation from the design.

PLA filament includes additional steps (drying and fermentation) that are not present for the production of other filaments, accounting for the larger impacts noted for ozone depletion potential and each of the ecotoxicity indicators. Transportation in between each of the steps as well as the energy consumption to perform the additional steps directly relate to the increased impacts that PLA has, and its production affects water depletion and local freshwater systems (relating directly to the ecotoxicity indicators that it leads in compared to the other polymers analyzed [40]). On the other hand, the production of nylon involves fewer steps: the extraction of raw materials such as adipic acid and hexamethylenediamine (from refined crude oil) is done, which then undergoes a condensation polymerization process to form nylon [40–43].

Renewable energy would help improve GHG emissions of PLA production. Additionally, the disposal phase is not considered in this analysis and this is where PLA could potentially have a greater advantage given that it is biodegradable. Vascular networks printed with ABS filament had the lowest impacts in seven of the ten categories, while vascular networks printed with nylon filament overall had the largest impacts in five of the ten categories evaluated. Nylon having significantly higher impacts in abiotic depletion, global warming potential, photochemical oxidation, acidification and eutrophication is expected, since those impacts involve the depletion of fossil fuels and their effects on the environment.

Overall, there is no clear benefit of using a vascular network of any material that is investigated here over manual repair when only one maintenance activity is considered. When additional repair is needed, the environmental effects related to the transportation of a lift and its power requirements become more pronounced relative to using a vascular network over multiple cycles, giving a vascular network system a definite advantage. The production of polymeric materials is not environmentally friendly, even for a non-fossil fuel based polymer such as PLA, but over time the overall impact of using a vascular network self-healing system compared to manual repair becomes reduced for PLA (Fig. 20) as well as each polymer type starting at the second repair action (Fig. 21), and significantly reduced after five repair actions (Fig. 22).

4. Conclusions

This demonstration highlighted the practicability of scaling up a ductile-porous vascular network for self-healing concrete. Potential construction challenges that may arise under realistic conditions were identified, and embedded and external sensors were employed to oversee the curing process and crack development of the walls. Damage and healing could be assessed, and a life cycle assessment was performed to compare the environmental impacts of a self-healing wall to a traditional manually repaired wall.

An extruded PU tube material was found to be a viable alternative to 3D printed filaments for a ductile-porous network, with no relative adverse effects to the concrete strain development. Thus, this is a suitable fabrication method for scaling-up a vascular network given the time savings it has for production. Numerical modelling with LUSAS was able to successfully predict curing and cracking patterns in realistic conditions.

Curing and damage can be effectively monitored using embedded sensors, however, for sensitive strain measurements, routine construction activities nearby can affect the readings. UPV is an effective non-destructive technique to track damage and correlate it with crack widths. A smaller grid size for taking UPV measurements can provide greater accuracy in tracking damage, as well as performing measurements in both horizontal and vertical directions.

Even with certain constructability issues that are easily mitigated (such as using more rigid polymeric tubing or additional connection points), a scaled-up ductile-porous vascular network can reach exceptionally high sealing efficiencies. Further network development and care during on-site installation is necessary for complete success of the system.

Finally, an LCA analysis indicated that while a one-time maintenance activity using a vascular network does not provide significant environmental benefits over manual repair, environmental impacts are greatly reduced when multiple repair actions are involved. For the case scenario studied here, the impacts from two repair actions using a vascular network begin to overcome the impacts of manual repair, and a substantial difference is noted for additional repair works. A full LCA would be an important step for future research as the technology matures and more comprehensive data become available, as it would provide a more complete picture of the environmental impacts and enhance the sustainability of the final product.

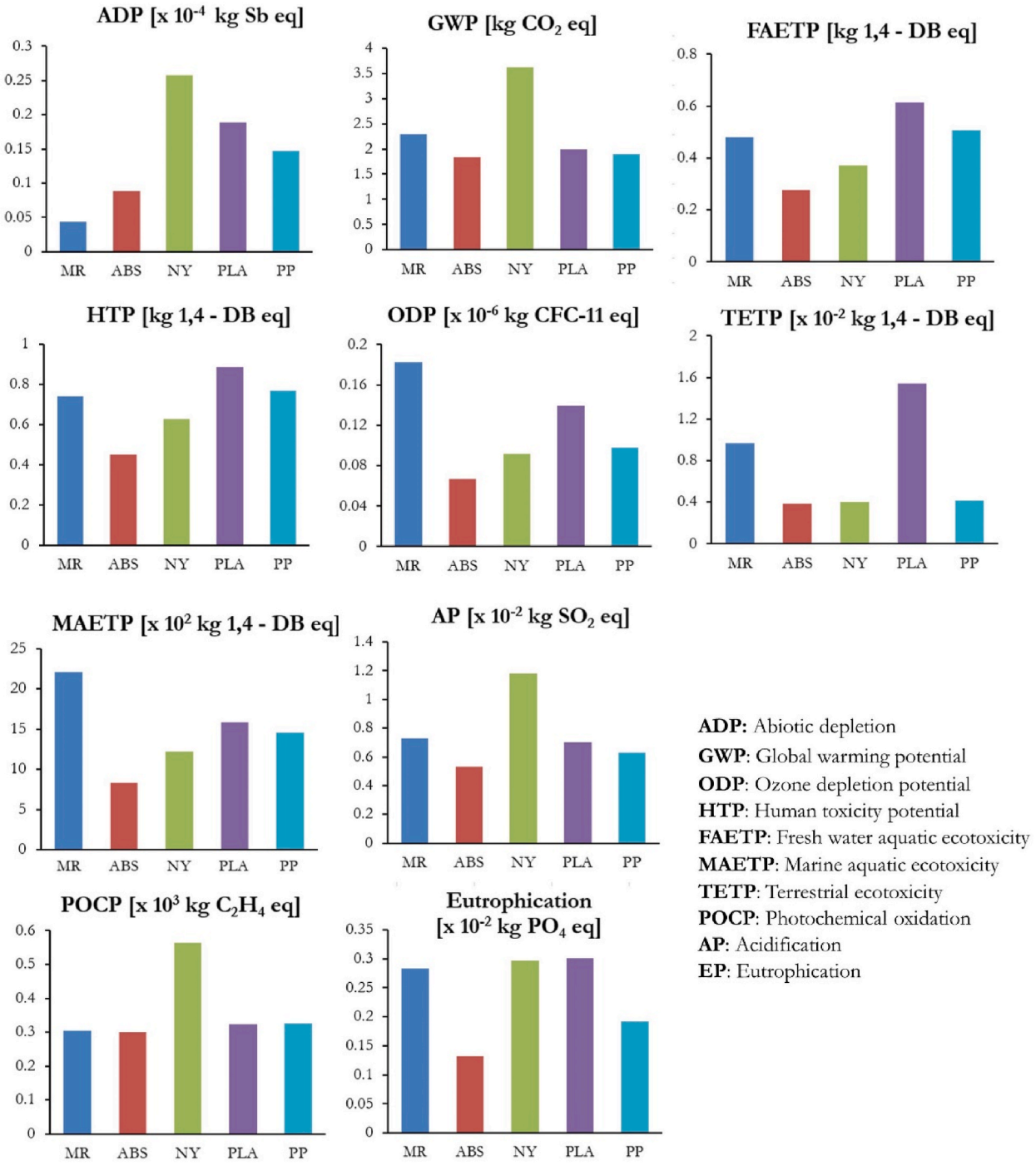

Fig. 18. LCA outcomes for one maintenance activity for manual repair (MR), and vascular networks whose branched parts are made with ABS (ABS), nylon (NY), PLA (PLA), or PP (PP).

CRediT authorship contribution statement

Yasmina Shields: Writing – review & editing, Writing – original draft, Visualization, Validation, Software, Methodology, Investigation, Formal analysis, Data curation, Conceptualization. **Davide di Summa:** Writing – review & editing, Software, Methodology, Investigation, Data curation. **Nicolas Ospitia:** Writing – review & editing, Methodology, Investigation, Conceptualization. **Gontran Herrier:** Writing – review & editing, Supervision, Resources, Methodology, Investigation, Conceptualization. **Erik Schlangen:** Writing – review & editing, Methodology, Conceptualization. **Tony Jefferson:** Writing – review & editing, Supervision, Software,

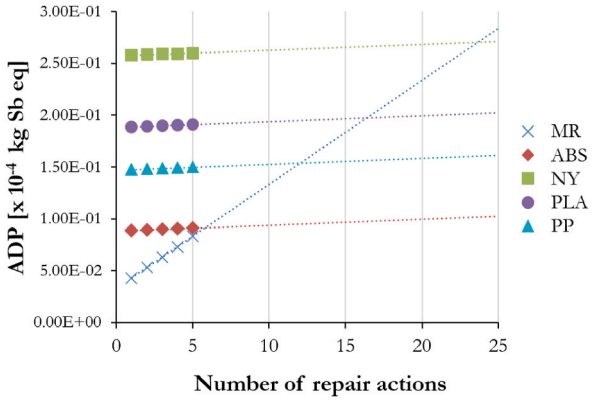

Fig. 19. Abiotic depletion potential over multiple maintenance activities; linear trendlines represent the forecasted impacts until 25 repair actions.

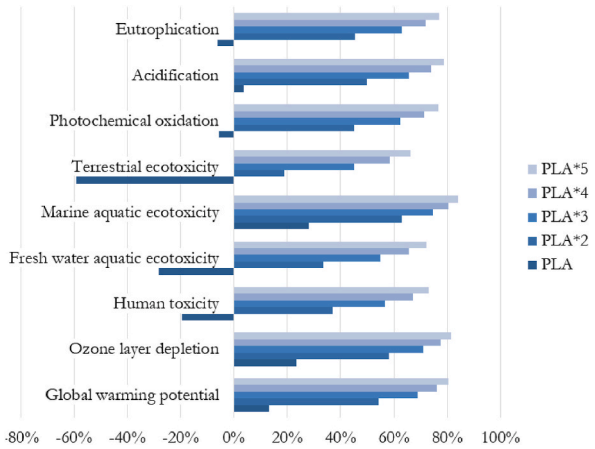

Fig. 20. Relative difference on environmental impacts of using a PLA vascular network over manual repair between one and five maintenance activities.

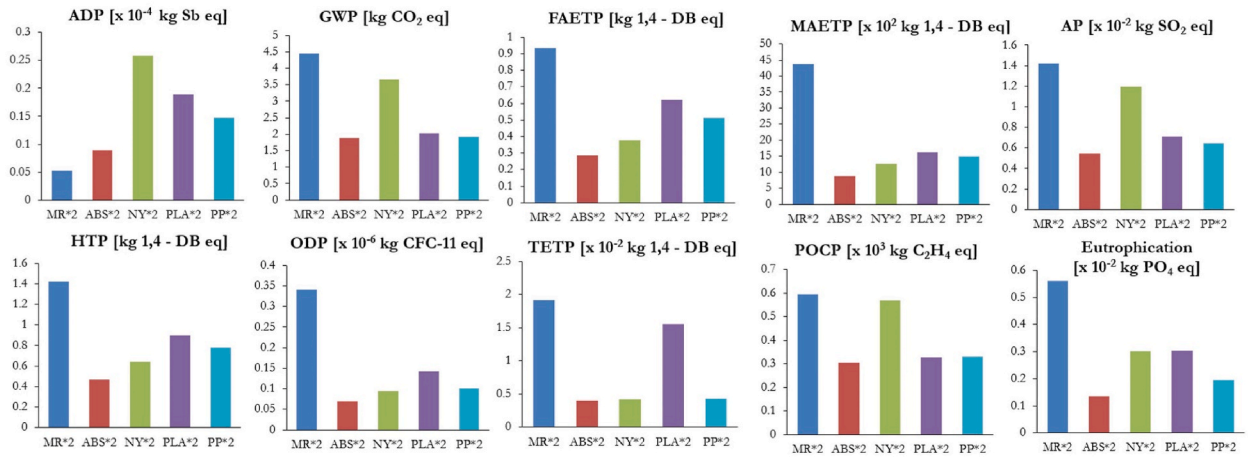

Fig. 21. LCA outcomes for two maintenance activities for manual repair (MR), and vascular networks whose branched parts are made with ABS (ABS), nylon (NY), PLA (PLA), or PP (PP).

Methodology, Investigation, Formal analysis, Conceptualization. **Nele De Belie:** Writing – review & editing, Validation, Supervision, Software, Resources, Project administration, Methodology, Investigation, Funding acquisition. **Kim Van Tittelboom:** Writing – review & editing, Validation, Supervision, Software, Resources, Project administration, Methodology, Investigation, Funding acquisition,

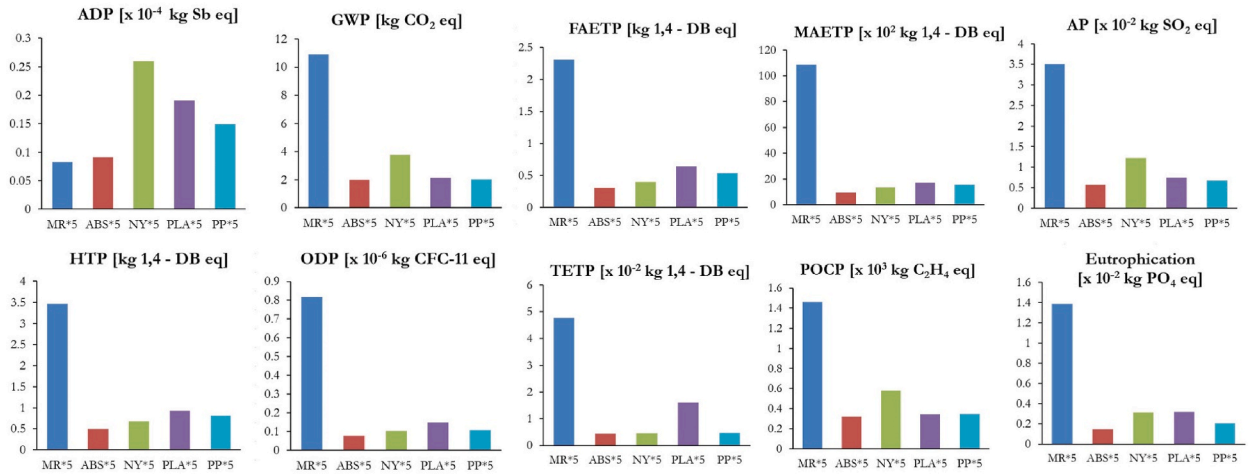

Fig. 22. LCA outcomes for five maintenance activities for manual repair (MR), and vascular networks whose branched parts are made with ABS (ABS), nylon (NY), PLA (PLA), or PP (PP).

Conceptualization.

Declaration of competing interest

The authors declare that they have no known competing financial interests or personal relationships that could have appeared to influence the work reported in this paper.

Data availability

Supplementary material can be found on Zenodo: 10.5281/zenodo.12510695.

Acknowledgements

Aid in the planning and construction from the BESIX personnel and the Henneaulaan Bridge project team is gratefully acknowledged, particularly from: Gontran Herrier, Jaques van Niekerk, and Christoph Klingeleers.

Technical assistance from the Magnel-Vandepitte Laboratory is also acknowledged, particularly from Nathan Lampens, Dieter Hillewaere, Stefan De Bock, and Lennert Cruypeninck. This work acknowledges funding from the SMARTINCS project. This project has received funding from the European Union's Horizon 2020 research and innovation programme under the Marie Skłodowska-Curie grant agreement no. 860006.

References

[1] C. De Nardi, D. Gardner, A.D. Jefferson, Development of 3D printed networks in self-healing concrete, Materials 13 (6) (Mar. 2020), https://doi.org/10.3390/ma13061328.
[2] Z. Li, L.R. De Souza, C. Litina, A.E. Markaki, A. Al-tabbaa, A novel biomimetic design of a 3D vascular structure for self-healing in cementitious materials using Murray ' s law, Mater. Des. 190 (2020) 108572, https://doi.org/10.1016/j.matdes.2020.108572.
[3] Y. Shields, T. Van Mullem, N. De Belie, K. Van Tittelboom, An investigation of suitable healing agents for vascular-based self-healing in cementitious materials, Sustainability 13 (23) (2021), https://doi.org/10.3390/su132312948.
[4] E. Tsangouri, C. Van Loo, Y. Shields, N. De Belie, K. Van Tittelboom, D.G. Aggelis, Reservoir-vascular tubes network for self-healing concrete: performance analysis by acoustic emission, digital image correlation and ultrasound velocity, Appl. Sci. 12 (10) (2022), https://doi.org/10.3390/app12104821.
[5] P. Minnebo, et al., A novel design of autonomously healed concrete: towards a vascular healing network, Materials 10 (1) (2017) 1–23, https://doi.org/10.3390/ma10010049.
[6] Z. Wan, Y. Xu, Y. Zhang, S. He, B. Šavija, Mechanical properties and healing efficiency of 3D-printed ABS vascular based self-healing cementitious composite: experiments and modelling, Eng. Fract. Mech. 267 (September 2021) (2022), https://doi.org/10.1016/j.engfracmech.2022.108471.
[7] C. De Nardi, D. Gardner, D. Cristofori, L. Ronchin, A. Vavasori, T. Jefferson, Advanced 3D printed mini-vascular network for self-healing concrete, Mater. Des. 230 (Jun. 2023) 111939, https://doi.org/10.1016/J.MATDES.2023.111939.
[8] C. De Nardi, et al., Experimental investigation of a novel formulation of a cyanoacrylate-based adhesive for self-healing concrete technologies, Front. Built Environ. 7 (Jun) (2021), https://doi.org/10.3389/fbuil.2021.660562.
[9] Y. Shields, et al., Non-destructive evaluation of ductile-porous versus brittle 3D printed vascular networks in self-healing concrete, Cem. Concr. Compos. 145 (Jan) (2024), https://doi.org/10.1016/j.cemconcomp.2023.105333.
[10] V. Kannan, Strength and durability performance of self compacting concrete containing self-combusted rice husk ash and metakaolin, Construct. Build. Mater. 160 (Jan. 2018) 169–179, https://doi.org/10.1016/j.conbuildmat.2017.11.043.
[11] W.E. Elemam, A.H. Abdelraheem, M.G. Mahdy, A.M. Tahwia, Optimizing fresh properties and compressive strength of self-consolidating concrete, Construct. Build. Mater. 249 (Jul) (2020), https://doi.org/10.1016/j.conbuildmat.2020.118781.
[12] Y. Shields, C. De Nardi, V. Cappellesso, T. Jefferson, N. De Belie, K. Van Tittelboom, A comparison of brittle versus ductile vascular networks: why ductile networks are preferable for scaling up, in: Proceedings of 8th International Conference on Self-Healing Materials, Milan, Italy, June 20th to 22nd, 2022, p. 178.

[13] C. Dry, Service Repair of Highway Bridges and Pavements by Internal Time-Release Repair Chemicals, INNOVATIONS DESERVING EXPLORATORY ANALYSIS (IDEA) PROGRAMS MANAGED BY THE TRANSPORTATION RESEARCH BOARD (TRB), 2001.
[14] C.M. Dry, Repair and prevention of damage due to transverse shrinkage cracks in bridge decks, in: Smart Structures and Materials 1999: Smart Systems for Bridges, Structures, and Highways, 1999, https://doi.org/10.1117/12.348675.
[15] R. Davies, et al., Large scale application of self-healing concrete: design, construction, and testing, Front Mater. 5 (September) (2018) 1–12, https://doi.org/10.3389/fmats.2018.00051.
[16] E. Tsangouri, et al., Feasibility study on real-scale , self-healing concrete slab by developing a smart capsules network and assessed by a plethora of advanced monitoring techniques, Construct. Build. Mater. 228 (2019) 116780, https://doi.org/10.1016/j.conbuildmat.2019.116780.
[17] P. Bamford, Early-Age Thermal Crack Control in Concrete, vol 23, Construction Industry Research and Information Association(CIRIA), 2007.
[18] A.D. Jefferson, I.C. Mihai, R. Tenchev, W.F. Alnaas, G. Cole, P. Lyons, A plastic-damage-contact constitutive model for concrete with smoothed evolution functions, Comput. Struct. 169 (Jun. 2016) 40–56, https://doi.org/10.1016/j.compstruc.2016.02.008.
[19] Anton Schindler, Kevin Folliard, Influence of supplementary cementing materials on the heat of hydration of concrete, Proc., Advances in Cement and Concrete IX Conf. (2003).
[20] A. Jefferson, et al., Finite element crack width computations with a thermo-hygro-mechanical-hydration model for concrete structures, Eur. J. Environ. Civ. Eng. 18 (7) (Aug. 2014) 793–813, https://doi.org/10.1080/19648189.2014.896755.
[21] A.S. Chitez, A.D. Jefferson, Porosity development in a thermo-hygral finite element model for cementitious materials, Cement Concr. Res. 78 (Dec. 2015) 216–233, https://doi.org/10.1016/j.cemconres.2015.07.010.
[22] J. Kheir, et al., Early age autogenous shrinkage cracking risk of an ultra-high performance concrete (UHPC) wall: modelling and experimental results, Eng. Fract. Mech. 257 (Nov. 2021), https://doi.org/10.1016/j.engfracmech.2021.108024.
[23] "Historical weather data; www.weather.com." [Online]. Available: www.weather.com.
[24] National Society of Professional Engineers (NSPE) Code of Ethics.".
[25] C.D. Murray, A relationship between circumference and weight in trees and its bearing on branching angles, J. Gen. Physiol. 10 (5) (1927) 725–729, https://doi.org/10.1085/jgp.10.5.725.
[26] E. Vangansbeke, Y. Shields, N. De Belie, K. Van Tittelboom, E. Tsangouri, Autonomous healing by vascular networks: tracking of cracks interaction by Ultrasounds and Acoustic Emission, MATEC Web Conf. 378 (Apr. 2023) 04003, https://doi.org/10.1051/matecconf/202337804003.
[27] T. Van Mullem, et al., Addressing the need for standardization of test methods for self-healing concrete: an inter-laboratory study on concrete with macrocapsules, Sci. Technol. Adv. Mater. (2020), https://doi.org/10.1080/14686996.2020.1814117.
[28] D. di Summa, et al., Environmental and economic sustainability of crack mitigation in reinforced concrete with SuperAbsorbent polymers (SAPs), J. Clean. Prod. 358 (Jul) (2022), https://doi.org/10.1016/j.jclepro.2022.131998.
[29] Thermoplastic Polyurethane Elastomers (TPU) Elastollan®– Processing Recommendations." [Online]. Available: https://www.distrupol.com/Elastollan_Processing_Recommendations.pdf.
[30] C. Abeykoon, A. Mcmillan, and B. K. Nguyen, "Energy Efficiency in Extrusion-Related Polymer Processing: a Review of State of the Art and Potential Efficiency Improvements.".
[31] J. Deng, et al., Energy monitoring and quality control of a single screw extruder, Appl. Energy 113 (2014) 1775–1785, https://doi.org/10.1016/j.apenergy.2013.08.084.
[32] Genie Self-Propelled Scissor Lifts - Spec sheet." [Online]. Available: https://atpaccesshire.co.uk/assets/downloads/Genie1932Spec.pdf.
[33] Replacement battery for Genie scissor lift GS-2046 24V battery." [Online]. Available: https://akkusys.shop/en/batteries-by-application/lifting-platform/batteries/3100/replacement-battery-for-genie-scissor-lift-gs-2046-24v-battery-set.
[34] EPD as per ISO 14025 and EN 15804+A2: SIKA Products based on polyurethane or silane-modified polymer, group vol. 1." [Online]. Available: https://epd-online.com/EmbeddedEpdList/Download/14650.
[35] L. van Oers, J. Guinée, The abiotic depletion potential: background, updates, and future, Resources 5 (1) (Mar. 2016) 16, https://doi.org/10.3390/resources5010016.
[36] I. Dincer, Y. Bicer, 1.27 life cycle assessment of energy, in: Comprehensive Energy Systems, Elsevier, 2018, pp. 1042–1084, https://doi.org/10.1016/B978-0-12-809597-3.00134-6.
[37] E.T.H. Vink, K.R. Rábago, D.A. Glassner, P.R. Gruber, Applications of life cycle assessment to NatureWorks™ polylactide (PLA) production, Polym. Degrad. Stabil. 80 (3) (2003) 403–419, https://doi.org/10.1016/S0141-3910(02)00372-5.
[38] E. Rezvani Ghomi, et al., The life cycle assessment for polylactic acid (PLA) to make it a low-carbon material, Polymers 13 (11) (Jun. 01, 2021), https://doi.org/10.3390/polym13111854. MDPI AG.
[39] P.T. Benavides, U. Lee, O. Zarè-Mehrjerdi, Life cycle greenhouse gas emissions and energy use of polylactic acid, bio-derived polyethylene, and fossil-derived polyethylene, J. Clean. Prod. 277 (Dec) (2020), https://doi.org/10.1016/j.jclepro.2020.124010.
[40] O. Ulkir, Energy-consumption-based life cycle assessment of additive-manufactured product with different types of materials, Polymers 15 (6) (Mar. 2023), https://doi.org/10.3390/polym15061466.
[41] P. Ketan Vagholkar and C. K. Parth Vagholkar, "Nylon (Chemistry, Properties and Uses) Effect of Composition and Film Thickness on the Properties of Automotive Interior Clear Coats View project Original Research Paper Nylon (Chemistry, Properties and Uses)." [Online]. Available: https://www.researchgate.net/publication/310951621.
[42] A. Tomasini, H.H. León-Santiesteban, Nylon uses in biotechnology, in: Biocomposites: Design and Mechanical Performance, Elsevier Inc., 2015, pp. 319–346, https://doi.org/10.1016/B978-1-78242-373-7.00006-8.
[43] L. Tonucci, A. Mascitti, A.M. Ferretti, F. Coccia, N. d'Alessandro, The role of nanoparticle catalysis in the nylon production, Catalysts 12 (10) (Oct. 2022), https://doi.org/10.3390/catal12101206.